Interaction of NO_x Reduction and Soot Oxidation in a DPF with Cu-Zeolite SCR Coating

E. Tronconi[1] · I. Nova[1] · F. Marchitti[1] · G. Koltsakis[2] · D. Karamitros[3] · B. Maletic[4] · N. Markert[4] · D. Chatterjee[4] · M. Hehle[4]

Received: 19 December 2014 / Revised: 2 April 2015 / Accepted: 14 April 2015

✉ N. Markert
norbert.markert@mtu-online.com

[1] LCCP, Dipartimento di Energia, Politecnico di Milano, Via La Masa 34, 20156 Milan, Italy

[2] Laboratory of Applied Thermodynamics, Aristotle University Thessaloniki, 54124 Thessaloniki, Greece

[3] Exothermia S.A., PO Box 4221, 21 Antoni Tritsi str., 57001 Pylaia, Greece

[4] MTU Friedrichshafen GmbH, Maybachplatz 1, 88045 Friedrichshafen, Germany

Nomenclature A. Latin Letters

a_1	Constant in channel pressure drop correlation −
c_m	Molecular density of gas mol/m^3
C_1	Parameter for wall permeability correction −
C_2	Parameter for wall permeability correction −
C_4	Slip correction factor −
C_P	Specific heat capacity $J/(kg \cdot K)$
d_h	Hydraulic diameter of a channel m
D_{knud}	Knudsen diffusivity m^2/s
D_{mol}	Molecular diffusivity m^2/s
d_{pore}	Mean pore size m
f_w	Geometric parameter −
h	Heat transfer coefficient $W/(m^2 \cdot K)$
H	Heat source component W/m^3
k_p	Apparent permeability of particulate layer m^2
$k_{p,0}$	Permeability of particulate layer m^2
k_w	Apparent permeability of substrate m^2
$k_{w,0}$	Permeability of clean substrate m^2
n	Stoichiometric coefficient −
p_j	Partial pressure Pa
R	Universal gas constant $J/(mol \cdot K)$
R_k	Reaction rate mol/($m^3 \cdot s$)
S	Heat source term W/m^3

S_F Monolith specific surface area m^2/m^3
T Temperature K
t Time s
v Velocity m/s
w Dimension perpendicular to wall surface −
w_p Soot layer thickness m
w_w Wall thickness m
y_j Molar fraction −
z Axial coordinate along monolith m

B. Greek Letters

ΔH Reaction heat J/mol
ε Macroscopic void fraction −
ε_{pore} Porosity of the washcoat −
μ Dynamic viscosity $Pa \cdot s$
ρ Density kg/m^3
τ Tortuosity −

C. Subscripts and Superscripts

g Exhaust gas
j Species index
k Reaction index
s Solid
w Substrate wall

1 Introduction

The enforcement of stricter emission standards on a global level has given a tremendous impetus to the development of efficient aftertreatment technologies for the removal of NO_x and particulate matter (PM) from the diesel exhaust. Typically, the reduction of NO_x and PM emissions is performed by separate devices [1]. Selective catalytic reduction (SCR) systems have been demonstrated as an effective solution for controlling NO_x emissions from heavy-duty diesel engines [2], while diesel particulate filters (DPF) are nowadays a well-established technology to reduce PM emissions, with their application ranging from light- to heavy-duty powertrains, but also in non-road.

In order to decrease the number of components present in the exhaust line and the associated packaging volume and costs, or to bring the SCR catalyst closer to the engine to improve temperature behavior, there is great interest in combining various functionalities into one aftertreatment device [3]. Alternatively, the need to allow for higher engine-out NO_x emissions in order to improve fuel economy, especially for heavy-duty engines, necessitates an increase in SCR volume without significantly affecting the overall package size. To answer to those needs, catalyst manufacturers have recently focused on the development of combined SCR/DPF devices (often referred to as SCRF®, WSCR, or SDPF) in which the highly porous walls of the DPF are impregnated with SCR catalytic material. Such devices have been shown to have high NO_x conversion capabilities [1, 2, 4]. Cu- and Fe-zeolite-based catalysts are more appropriate and commonly used as SCR catalysts on DPF due to their higher thermal stability [5]. For light-duty applications, Cu-zeolite catalysts are more suitable due to the higher activity at low temperatures and the lower dependency on NO_2. Apart from the technological challenge of merging the deNO_x and PM control functionalities, the performance of the SCRF®, compared to that of the individual SCR and DPF devices, is a key aspect. The cross-interactions between the SCR and DPF functions for the general case of a soot-loaded SDPF must be considered [6–8]. Examples are the competitive NO_2 consumption by the SCR reactions and the passive soot oxidation or the trade-off that needs to be made when choosing the optimal washcoat amount to balance between deNO_x performance, filtration efficiency and pressure drop behavior. In addition, another aspect of the competitive interactions taking place in a wall-flow SCR is the effect of soot presence on NO_x conversion. Reaction of NO_2 with soot to form NO alters the in situ NO_2/NO_x ratio, which is known to be a controlling factor in the deNO_x performance. Depending on the operating conditions, this can result either in a promoting or a detrimental effect [6]. Finally, the thermally rougher conditions observed in filters impose more challenging requirements with respect to the thermal stability of SCR catalyst formulations [3].

Taking into account all the above aspects, the integration of the SCR and DPF functionalities into a single aftertreatment device poses a major technological challenge which requires extensive experimental work. The latter can be effectively supported by simulation tools whose application is nowadays well recognized as a cost- and time-efficient strategy during the development process.

The study herein presented has addressed both the intrinsic SCR and soot oxidation chemistries, as well as their mutual interactions. The resulting kinetic mechanisms have been implemented into an AxiSuite® SDPF model, and validated under real exhaust conditions against data from test runs of SDPF system with a PC engine, accounting also for pressure losses. Finally, the predictive potential of the SDPF model was successfully evaluated against the results of a measurement campaign at the full scale, based on tests with a MTU non-road engine.

2 Experimental and Methods

2.1 Lab-Scale Runs Over Powdered Catalyst

2.1.1 NH_3-SCR Kinetic Runs

SCR kinetic tests for the estimation of the rate parameters were performed over a commercial Cu-zeolite catalyst in the form of powder. To obtain the powder, the original washcoated wall-flow monolith (Cu-zeolite on DPF), after

removing plugs, was crushed and sieved to a particle size within the 95–106μm range, chosen to prevent the occurrence of bypass, mitigate the pressure drop, and afford operation in a chemical regime. In order to reduce the possibly different responses of the SCR active phase and of the wall-flow filter to the crushing process, the fraction of bigger particles from sieving were crushed and further sieved, while the fines were pelletized, crushed, and sieved again. This process was repeated until all the original crushed monolith powder was in the same desired mesh interval (95–106 μm).

The set of kinetic runs was performed in a fixed bed micro-reactor, consisting of a stainless steel tube (15 mm i.d.), loaded with crushed catalyst, and placed in an electric furnace which enabled either isothermal steady-state conditions or fast temperature-programmed transients. The reaction temperature was monitored and controlled by two K-type thermocouples placed in contact with the top and the bottom of the catalyst bed, respectively. Mass flow controllers (Brooks Instruments) were used to dose NH_3, NO, NO_2, O_2 (with N_2 as carrier gas) from bottles containing calibrated gas mixtures, whereas distilled water was dosed by a piston volumetric pump (Gilson, model 305). All the lines before and after the reactor were heated to 250 °C to prevent ammonium nitrate deposition. The NH_3, NO, NO_2 species concentrations in the reactor outlet stream were continuously monitored by a UV analyzer (ABB Limas 11HW), while the N_2O outlet concentration was measured by a dedicated ND-IR ABB Uras 14 analyzer. Since H_2O could affect the N_2O analysis by IR, a SCC-C ABB condenser was placed just upstream of the ND-IR analyzer.

Prior to the kinetic runs, the catalyst was conditioned by heating it up to 550 °C in the presence of 10 % *v*/*v* of both O_2 and H_2O; it was then held at 550 °C for 5 h and eventually cooled down to room temperature in the same gaseous stream. The runs used for kinetic model development were performed at atmospheric pressure under both steady-state and transient conditions, with typical feed concentrations of 0–500–1000 ppm for NH_3 and 0–500 ppm for NO and NO_2 in a base feed stream consisting of 5 % (*v*/*v*) H_2O and balance N_2. The effects of the following operating conditions were investigated in steady-state runs: GHSV (30,000–100,000–150,000 h^{-1}), O_2 feed content (2–8 % *v*/*v*), and NO_2/NO_x feed ratio (0–1), keeping the NH_3/NO_x feed ratio alpha=1. The effects of the NH_3 adsorption temperature (150–200 °C) and of the NH_3 feed concentration (500–1000 ppm) on the ammonia adsorption-desorption behavior were also addressed as key variables for a complete identification of the SCR reaction scheme.

2.1.2 Lab-Scale NH_3-SCR + Soot Combustion Runs

The same commercial Cu-zeolite catalyst was further tested in the form of powder mixed with soot particles in order to study the mutual interactions between the soot combustion and NH_3-SCR chemistries. A different microflow reactor rig was used in this case. The SCR activity was first investigated in a preliminary set of steady-state runs to provide a baseline for the tests involving the coupled reacting systems. The catalytic bed for the SCR activity runs included 70 mg of crushed Cu-SDPF and 70 mg of inert uncoated powdered cordierite as a diluent.

A real soot, named LAT-soot in the following, was used for SCR + soot combustion runs. It was generated at LAT running a Daimler OM646 diesel and collecting it in an uncoated DPF. The extraction of the soot was achieved by reverse blowing of the uncoated DPF. The engine is described later. To mitigate the impact of volatile organic compounds (VOC) on the soot activity, the LAT-soot was collected after a DOC. The soot particulate was added to the catalyst powders and then well mixed with a spatula (loose contact methodology). The bed composition in all these runs was as follows: powdered Cu-SDPF:Cordierite:Soot 10:10:1. The so-prepared physical mixture (LAT-soot + Cu-SDPF + cordierite) was loaded in a flow micro-reactor consisting of a quartz tube (6 mm i.d.) placed in an electric furnace with a thermocouple directly immersed in the catalyst bed to measure the reaction temperature. During each run, the whole load of soot was completely burned out. Accordingly, a new reactor had to be prepared for every NH_3-SCR + soot combustion run. NH_3, NO, NO_2, O_2, and He (carrier gas) were dosed from calibrated gas mixtures via mass flow controllers, while water vapor was added by means of a saturator. The reactor outlet was directly connected to three gas analyzers in parallel, namely a quadrupole mass spectrometer (Balzers QMS 200), for analysis of N_2O, NO, NO_2, N_2, and H_2O; a UV analyzer (ABB Limas 11HW), for analysis of NO, NO_2, and NH_3; and a ND-IR analyzer (ABB Uras 14) for analysis of CO and CO_2.

In the case of soot combustion runs, both isothermal steady-state experiments and temperature-programmed reaction (TPR) experiments were performed within the 150–500 °C and 150–700 °C T ranges, respectively; the heating rate in TPR runs was 2 °C/min. Typical feed concentrations of NO_x (with $0 \le NO_2/NO_x \le 1$) and NH_3 were 500 ppm, in the presence of O_2 (8 % *v*/*v*) and H_2O (5 % *v*/*v*) with balance He. A more detailed description of the experimental rig and procedures can be found in [9, 10]. After each run, the C balance was evaluated according to the following equation:

$$\text{Carbon balance } \% = 100 \cdot \frac{\text{mol}_{CO_x} \cdot \text{MW}_{\text{Carbon}}}{m_{\text{LAT-soot}}} \qquad \text{(E.1)}$$

where mol_{COx} represents the cumulative number of moles of $CO + CO_2$ released during the runs, obtained by integration of the CO_x curves, while $m_{\text{LAT-soot}}$ is the mass of soot initially loaded in the reactor.

The two sets of runs, with and without LAT-soot powder, were performed at different volumetric flows but at the same GHSV (150,000 h^{-1}) to enable direct comparison of the results.

2.1.3 NH_3-SCR Kinetic Model

A recent comprehensive literature, kinetic mechanism [11] was used to fit the whole set of lab-scale NH_3-SCR kinetic runs. Considering that the literature model had been originally developed for a Fe-zeolite catalyst, it was necessary to modify it in order to comply with the typical, slightly different behavior of Cu-zeolite catalysts [12] as follows:

- there is no overconsumption of NH_3 in standard SCR over Cu-zeolites: accordingly, the NO promotion of NH_3 oxidation was disregarded;
- there is no inhibition of NH_3 in standard SCR over Cu-zeolites: accordingly, the "spillover" of NH_3 onto redox sites was eliminated;
- the N_2O reactivity with NO and NH_3 is negligible over Cu-zeolites: it was therefore disregarded.

The kinetic mechanism was fitted to the lab-scale NH_3-SCR runs by multi-response non-linear regression, based on the least squares method, assuming a time-dependent, isothermal, isobaric plug-flow model of the microflow test reactor. Details of the procedure can be found in [12].

2.2 Medium-Scale Engine Tests

2.2.1 Methodology

Following a scale-up approach, intrinsic SCR reaction kinetics previously determined from micro-reactor tests were directly transferred to full-scale monolithic converters. Engine bench experiments were conducted at the Laboratory of Applied Thermodynamics (LAT) of Aristotle University of Thessaloniki (AUTh) in order to validate the SCR kinetic model under real exhaust conditions, and to calibrate the DPF model with respect to the filtration/pressure drop behavior and to the soot oxidation kinetics. Additionally, dedicated experiments were conducted in order to study the interaction between NO_x conversion and soot oxidation as well as to evaluate the model's ability to predict the observed trends.

For the purposes of this study, the AxiSuite® commercial software platform was used in order to model the SDPF performance related to NO_x conversion, pressure drop, and soot oxidation. The main wall-flow filter model equations for the mass-momentum, energy, and species balances are analytical-ly described in the Appendix.

2.2.2 Experimental Test Description

The tests were performed on engine dyno with a 2.2 l Euro 4 engine (Daimler OM 646). Even though the engine and the exhaust system components are downsized compared to the targeted application, the operating conditions were selected to allow proper scale-up to the final application. The exhaust system setup is schematically presented in Fig. 1.

A 5.66×10 in. Cu-zeolite SDPF filter was used in the measurements. Depending on the test protocol, either a DOC or a catalyzed DPF was placed upstream of the SDPF. Ammonia injection was performed in gaseous form via a proper three-probe configuration in order to ensure good NH_3 uniformity in the exhaust gas. The required amount of NH_3 flow was controlled externally via a mass flow controller. SDPF inlet NO and NO_x concentrations were measured with a Horiba PG-250 analyzer and a NO_x sensor, respectively. In the SDPF outlet, $NO/NO_2/NH_3$ concentrations were recorded with an ABB Limas 11HW analyzer. An AVL Micro Soot Sensor was used to monitor SDPF inlet/outlet soot emissions and to measure the filtration efficiency.

Experiments can be categorized to (i) measurements for model calibration and (ii) measurements for model validation. The first includes clean and loaded pressure drop experiments at various flow rates and passive regeneration tests at various temperatures. Model validation tests consist of passive regeneration experiments with simultaneous NH_3 injection in order to verify the ability of the model to predict the SCR effect on the soot consumption rate.

Typical steady-state test protocols for soot loading and passive regeneration experiments are presented in Fig. 2.

A summary of the experimental protocols and the respective test conditions is given in Table 1. The application of a cDPF upstream the SDPF was chosen during passive regeneration tests. In this way it was possible to avoid additional soot accumulation and at the same time to have a realistic inlet NO_2/NO_x ratio.

2.3 Adjustment to Full-Scale Non-Road Application

After finishing the validation of the SCR kinetics and DPF calibration under real exhaust conditions with data from a PC engine (OM646), the so-received SDPF model was evaluated against the results of a SDPF measurement campaign over a Cu-zeolite on a different type of DPF substrate at a MTU non-road engine. The first results clearly show not only an impact of substrate type to the specific DPF characteristic due to changes in wall permeability, but also an influence of the specific soot characteristic of the engine on the soot oxidation kinetics. To fit the model to the appropriate MTU application, several experiments were conducted to adjust the relevant parameters of the SDPF model. The test bench setup at MTU is schematically illustrated in Fig. 3.

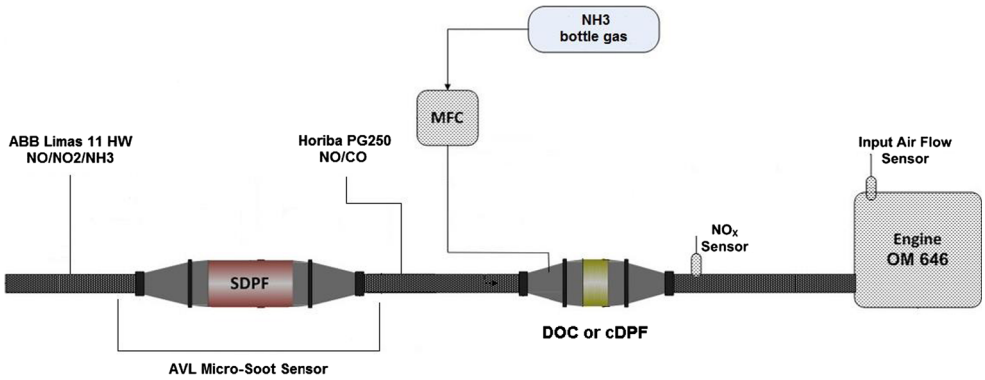

Fig. 1 Experimental setup

These tests were performed with a MTU non-road engine. Depending on the test protocol, a DOC or a catalyzed DPF was placed upstream the SDPF. For SCR reaction, an appropriate amount of urea was dosed, decomposed, and intensely mixed with exhaust gas to ensure high uniformity of the reducing agent. The design of exhaust piping is specific for engine tests to ensure almost ideal boundary conditions for catalytic investigations and emission measurements. All regulated gaseous emissions (NO, NO_x, CO, THC) were measured up- and downstream the SDPF with an AVL AMA i60. Secondary emissions (like N_2O and NH_3) were monitored with an AVL SESAM FTIR. For calculating filtration efficiency and soot loading, an AVL Micro Soot Sensor was applied up- and downstream the SDPF, recording the soot emissions.

The performed experiments for adaptation of SDPF model to MTU specific application were comparable to those conducted at LAT laboratory (pressure drop and filtration efficiency; soot oxidation with and without reducing agent). A more detailed summary of the experimental protocols and respective conditions is given in Table 2. The application of a cDPF upstream the SDPF was chosen during passive regeneration tests. In this way, it was possible to avoid additional soot accumulation, and at the same time, to have a realistic inlet NO_2/NO_x ratio.

3 Results and Discussion

3.1 NH_3-SCR Activity of Cu-Zeolite and Mutual Interactions with Soot Combustion

3.1.1 NH_3-SCR Kinetic Runs and Rate Model Fit

Since it is well known that the deNO_x performances as well as the dynamics of SCR converters are driven by the reactivity of adsorbed NH_3, the first step in the development of the kinetic mechanism involved the evaluation of the NH_3 adsorption/desorption rates on the Cu-zeolite surface, which were studied by two-stage runs. In the first isothermal stage, NH_3 was stepwise fed to the reactor, enabling both the adsorption and desorption of weakly adsorbed ammonia (or physisorbed ammonia). In the second stage, a temperature ramp was performed to desorb strongly adsorbed ammonia (or chemisorbed ammonia) (temperature-programmed desorption (TPD)). At this purpose, three dedicated runs were performed, varying both the NH_3 feed content and the adsorption temperature from 500 to 1000 ppm and 150 to 200 °C, respectively, both variables affecting the interaction of NH_3 with the catalyst surface. For such three runs, Fig. 4 displays a zoom of the TPD section, comparing measured and fitted NH_3 concentrations: a good match between experimental TPD traces (symbols + thin lines) and model predictions (solid lines) is clearly apparent.

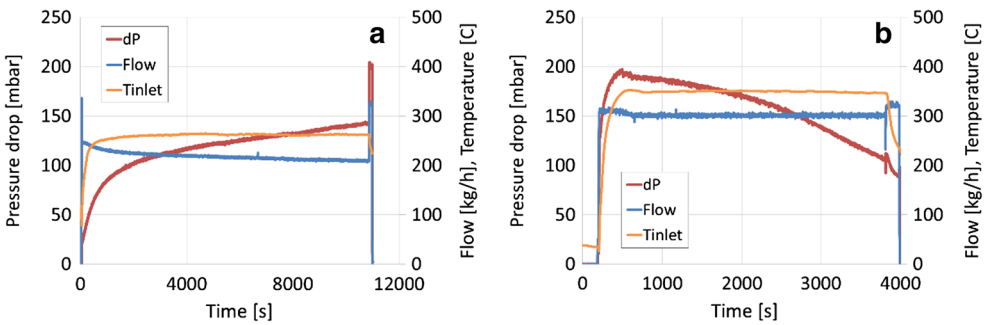

Fig. 2 Typical test protocols for **a** soot loading and **b** passive regeneration experiments

Table 1 Summary of experiments and respective test conditions

Condition experiment	Temperature [°C]	Flow rate [kg/h]	Upstream device
Clean filter pressure drop	200–400	30–400	cDPF
Soot loading and filtration	220–260	70, 150, 230	DOC
Passive regeneration without NH_3	350, 450	Depending on test	cDPF
Passive regeneration with NH_3 (α=1.05)	350, 450	Depending on test	cDPF

Table 2 Summary of experiments and test conditions

Condition experiment	Temperature [°C]	Flow rate [kg/h]	Upstream device
NO_x conversion without soot (variation of α)	230–400	550–1900	cDPF
Soot loading and filtration	230	1000	DOC
Passive regeneration without NH_3	400	1850	cDPF
Passive regeneration with NH_3 (α=1.0)	400	1850	cDPF

The kinetic model was further calibrated against a set of steady-state experiments that included three NH_3 oxidation, three standard SCR, two fast SCR, two NO_2 SCR runs, and two additional SCR runs with intermediate NO_2/NO_x feed ratios (0.25 and 0.75).

The experimental and fitted data for the NH_3 oxidation run are plotted in Fig. 5a, showing a satisfactory match. For a standard SCR run, Fig. 5b confirms the adequacy of the fit in the whole temperature range; at high temperatures, the NO slip is well reproduced also, thanks to the nice fit obtained for the NH_3 oxidation, which is responsible for the divergence from the 1:1 NH_3/NO molar ratio observed at T >350 °C. With respect to the fast SCR reacting system shown in Fig. 5c, we notice a slight underestimation of the low-temperature activity (until 250 °C), while the fit well reproduces the NO slip in this case, too. Finally, the analysis of the NO_2 SCR reacting system is mandatory for modeling purposes (Fig. 5d) in order to characterize the catalyst performance over the full NO_2/NO_x range, even though it is not relevant for the practical application of SDPF so far as DOC and SDPF are matched in an appropriate manner. The fit accurately describes both the reactants conversion and the N_2O formation, except for the NO slip, which is underestimated at 500 °C.

3.1.2 Effect of NO_x on Soot Combustion

The next step in the fundamental part of this study involved the evaluation of the impact of NO_x as oxidizing species on the combustion of soot. For that purpose, a tailored set of soot combustion experiments in the presence of NO_x was designed, wherein the NO_2/NO_x molar feed ratio was increased from 0 to 1 with an intermediate value of 0.5. Such runs have been also later used as a reference for the soot combustion when investigating the effect of the NH_3-SCR reactions on the soot oxidation chemistry.

The first investigated reacting system involved only O_2 as the oxidant: 8 % *v*/*v* of O_2 were added to a He stream with H_2O (5 % *v*/*v*) fed to the micro-reactor loaded with soot. The microflow reactor was heated up from 150 to 700 °C while the outlet concentration was continuously monitored. As expected [13], the O_2-driven soot combustion showed a very limited activity (Fig. 6a) below 400 °C, which represents a typical threshold temperature for the reactions between soot and O_2 over metal-exchanged zeolites [7]:

$$C + \frac{1}{2}O_2 \rightarrow CO \quad \text{(R.1)}$$

$$C + O_2 \rightarrow CO_2 \quad \text{(R.2)}$$

Higher temperatures enabled a rapid increase of the soot oxidation rate with an intense production of CO_2 and less abundant CO. The CO_x formation reached a maximum at 550 °C, with formation of 820 and 120 ppm of CO_2 and CO, respectively. The soot combustion was quantitatively completed at 600 °C.

Figure 6b shows the results of a similar soot combustion run, wherein 500 ppm of NO were added to the feed gas stream. Clearly, the addition of NO did not affect the soot reactivity [14]: in the whole temperature range, in fact, the CO_x formation was definitely comparable with the one seen in the absence of NO (Fig. 6a).

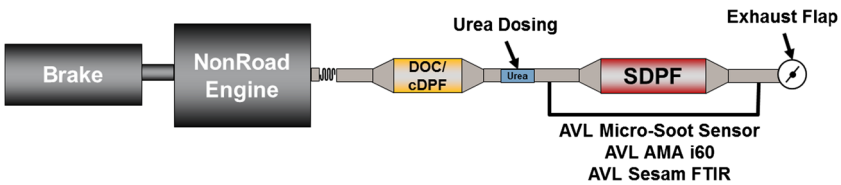

Fig. 3 Experimental setup of MTU test bench

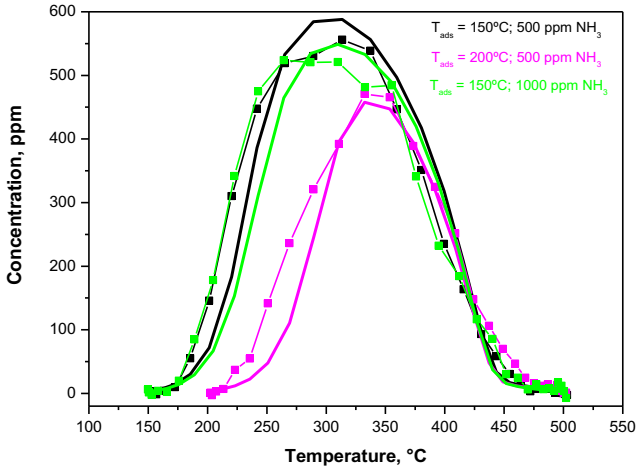

Fig. 4 Effects of adsorption temperature and NH_3 feed concentration on NH_3 TPD: experimental versus fitted data; GHSV=30,000 h^{-1}, C_{in} H_2O=5 %, C_{in} O_2=0 %, heating rate=40 K/min. *Thin lines with square symbols* represent the experimental data; *thick lines* represent kinetic fit

Further, the data in Fig. 6b indicate that NO is unable to interact/react with soot, as the NO concentration remained equal to its feed value.

Next, the soot combustion was studied upon feeding an equimolar NO-NO_2 mixture (250 ppm each). In view of the higher concentrations of CO_x detected below 400 °C (Fig. 6c), we can conclude that the presence of 250 ppm of NO_2 enhanced the low-temperature soot combustion due to the occurrence of [7, 14]:

$$C + NO_2 \rightarrow CO + NO \quad \text{(R.3)}$$

$$C + 2NO_2 \rightarrow CO_2 + 2NO \quad \text{(R.4)}$$

This is indeed confirmed by the data on the reactivity of NO_x: Fig. 6c shows clearly that conversion of NO_2 to NO is associated with the more pronounced CO_x formation below 400 °C: this is in line with R.3 and R.4. The high temperature peak of CO and CO_2 was still observed, however, meaning that NO_2 was unable to fully oxidize the entire soot load, so that the O_2-activated soot combustion pathway still played a role when NO_2 was a limiting reactant.

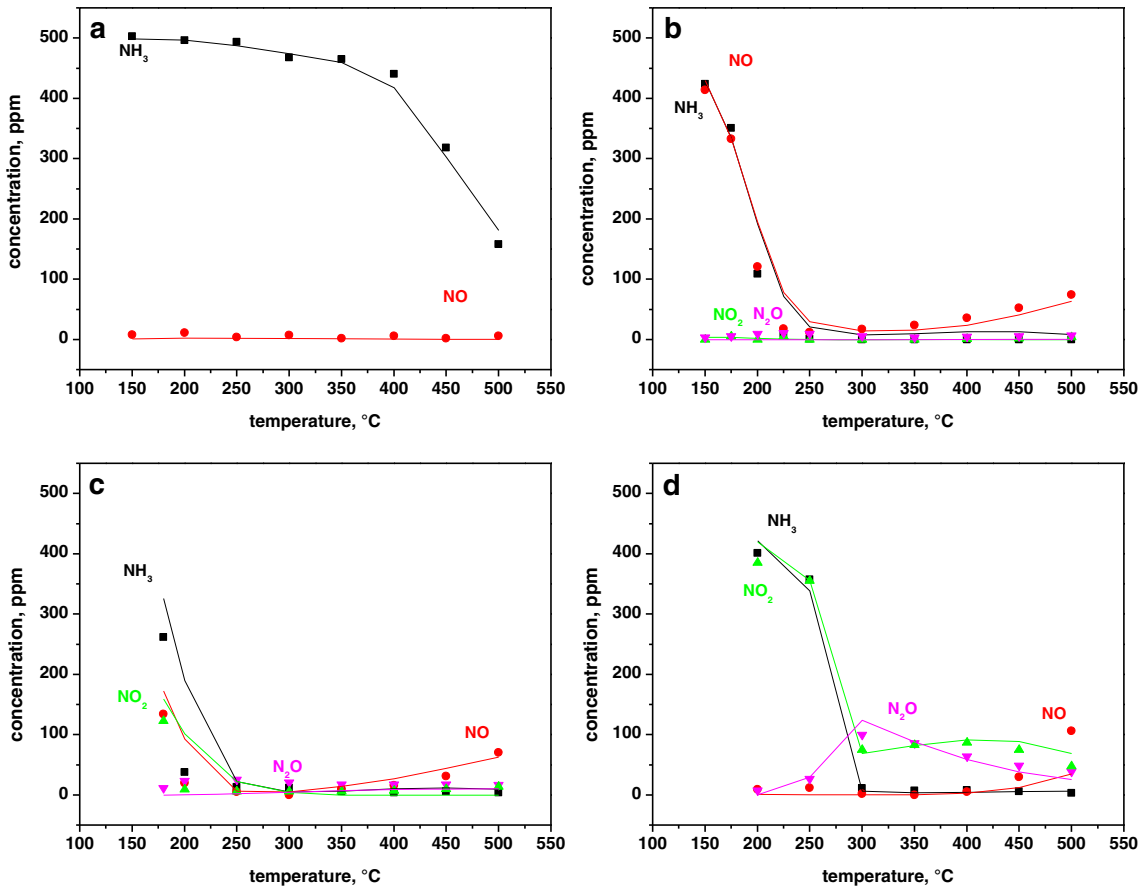

Fig. 5 NH_3-SCR steady-state kinetic runs: experimental (*symbols*) versus fitted (*solid lines*) data. GHSV=100,000 h^{-1}, H_2O=5 %. **a** NH_3 oxidation: C_{in} O_2=2 %, C_{in} NO_x=0 ppm; **b** Standard SCR: C_{in} O_2=8 %, C_{in} NO_x=500 ppm, NO_2/NO_x=0; **c** Fast SCR: C_{in} O_2=8 %, C_{in} NO_x=500 ppm, NO_2/NO_x=0.5; and **d** NO_2 SCR: C_{in} O_2=8 %, C_{in} NO_x=500 ppm, NO_2/NO_x=1

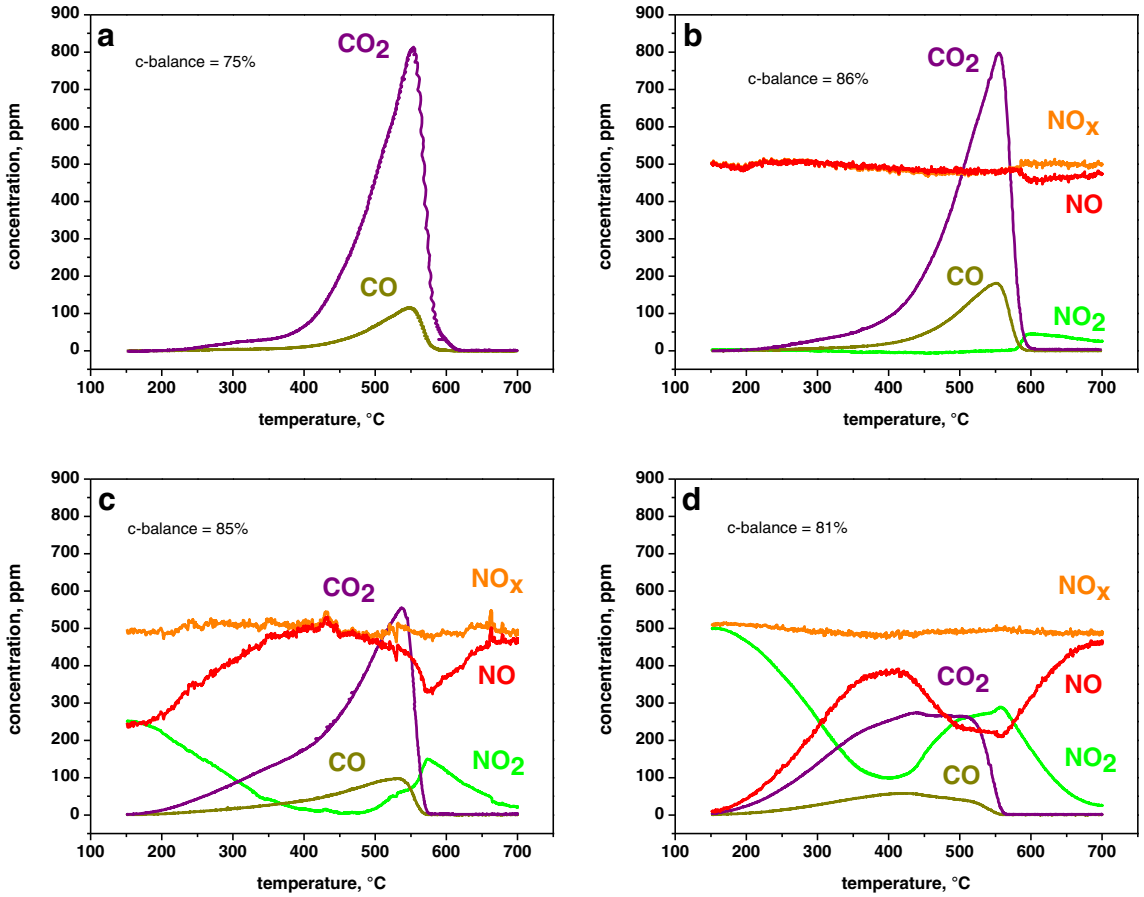

Fig. 6 Effect of NO_x on soot combustion. GHSV=150,000 h^{-1}, H_2O=5 %, C_{in} O_2=8 %. **a** NH_3 oxidation: C_{in} NO_x=0 ppm; **b** Standard SCR: C_{in} NO_x= 500 ppm, NO_2/NO_x=0; **c** Fast SCR: C_{in} NO_x=500 ppm, NO_2/NO_x=0.5; and **d** NO_2 SCR: C_{in} NO_x=500 ppm, NO_2/NO_x=1. Heating rate=2 K/min

In order to explore the limit of the NO_2-boosting effect, a dedicated run was performed adding 500 ppm of NO_2 only (NO_2/NO_x ratio equal to 1) to the reactor feed stream. The results are shown in Fig. 6d: upon doubling the NO_2 feed content, the low-temperature promotion of soot combustion was greater than in Fig. 6c. Soot oxidation started already at 250–300 °C. Furthermore, the soot combustion was completed around 550 °C without noticeable CO_x peaks. Inspection of the NO_2 and NO traces shows that the NO_2-assisted soot combustion peaked at 420 °C, but the extent of NO_2 conversion to NO dropped significantly above this temperature. We conclude that in this run, the oxygen combustion was still active between 420 and 550 °C, but it played a secondary role since most of the soot had been already oxidized by NO_2 at lower temperatures.

3.1.3 Effect of NH_3 + NO_x on Soot Combustion

As a final step in the fundamental part of the present study, also the impact of ammonia (both in the absence and in the presence of NO_x) on the soot combustion over the Cu-zeolite catalyst was addressed. This of course leads to explore as well the dual impact of the soot presence/reactivity on the NH_3-SCR deNO_x activity. The summary plot in Fig. 7 compares the CO_x profiles recorded in the four runs already shown in Fig. 6 to results from similar runs wherein 500 ppm of NH_3 were added to the reacting system.

In Fig. 7a both the CO_2 and the CO peaks recorded in the presence of NH_3 are shifted to slightly lower temperatures, roughly by 50 °C, suggesting that NH_3 had some counter intuitive but positive effect on the pure O_2-based soot combustion that still needs be elucidated. On the other hand, NH_3 did not affect the O_2-based soot combustion in the presence of NO (Fig. 7b). In summary, both the NH_3 oxidation and the standard SCR reaction, i.e., the reactions which proceeded during the runs with ammonia in Fig. 7a, b, have no adverse impact on the soot oxidation, and thus on the DPF regeneration.

On the contrary, big variations of the soot reactivity were detected when feeding 500 ppm of NH_3 together with a NO_2-containing NO_x mixture. Indeed, as shown in Fig. 7c, upon

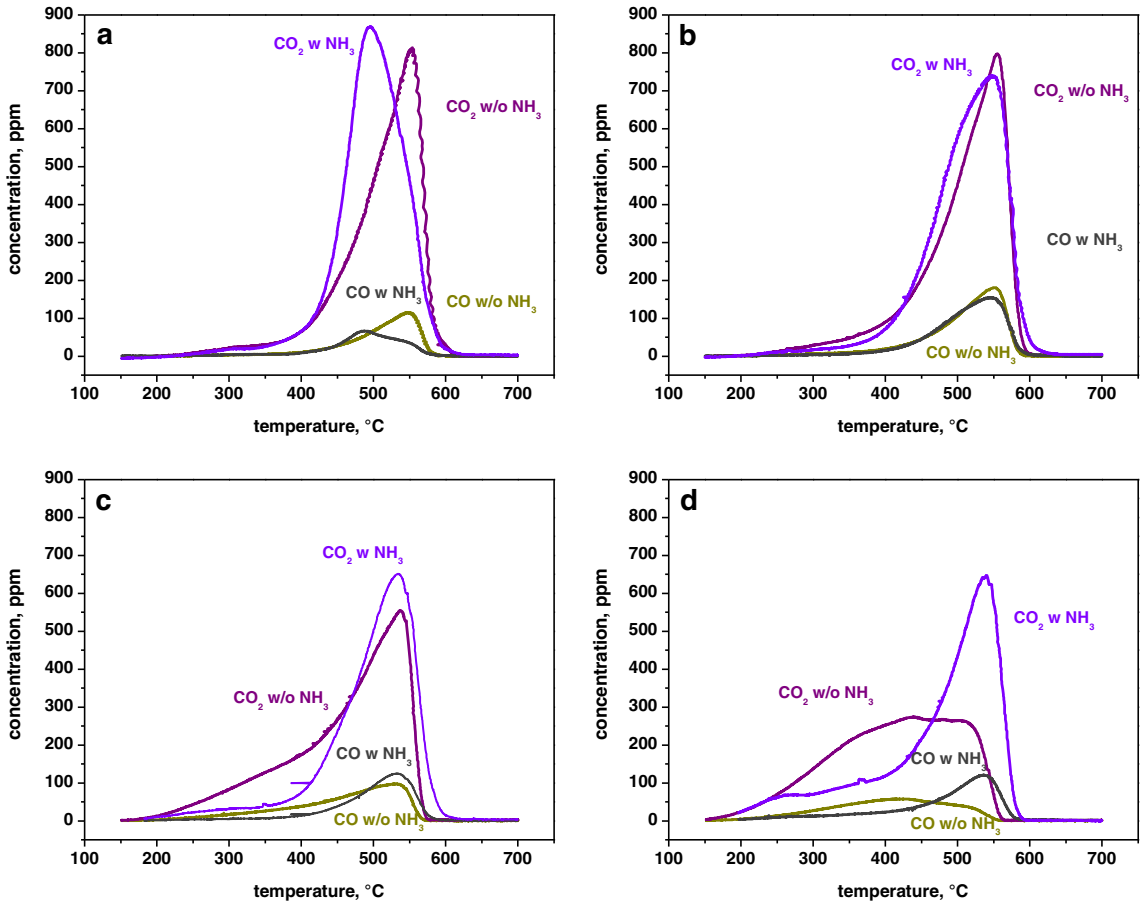

Fig. 7 Effect of NH_3 and NO_x on the soot combustion. GHSV=150,000 h^{-1}, H_2O=5 %, C_{in} O_2=8 %; when NH_3 is present: C_{in} NH_3=500 ppm. **a** C_{in} NO_x=0 ppm; **b** C_{in} NO_x=500 ppm, NO_2/NO_x=0; **c** C_{in} NO_x=500 ppm, NO_2/NO_x=0.5; and **d** C_{in} NO_x=500 ppm, NO_2/NO_x=1. Heating rate=2 K/min

feeding 500 ppm of NH_3 together with 250 ppm each of NO_2 and NO, the low-T soot reactivity was lowered, resulting in clearly reduced formation of CO and CO_2 in the mid- to low-temperature range: in the presence of NH_3 the CO_2 shoulder (purple line) between 200 and 450 °C completely disappeared. This effect is associated with the corresponding enlargement of the CO_2 peak at 550 °C (violet line), which suggests that the soot oxidation is primarily effected by O_2 rather than by NO_2. A similar trend is also evident in the runs of Fig. 7d, where NH_3 was added to a reacting system involving NO_2 as the

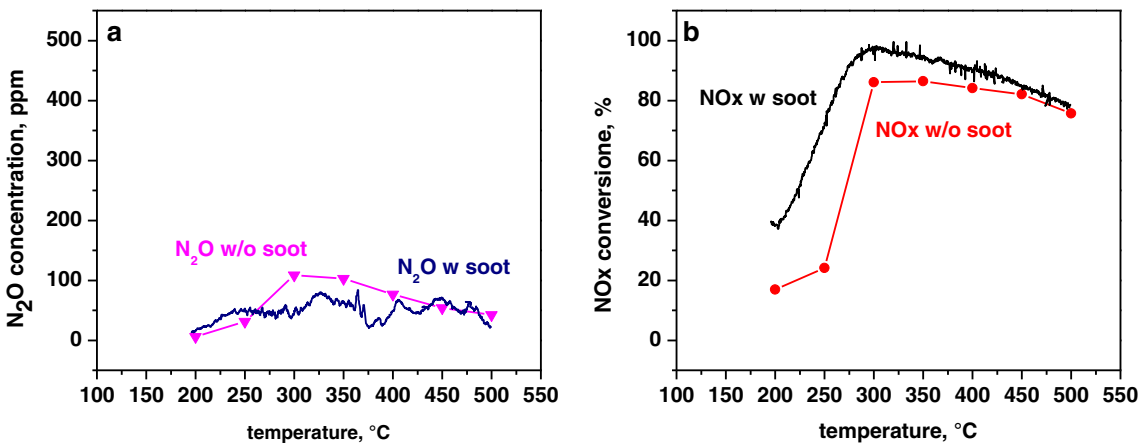

Fig. 8 Effect of soot on NO_2-SCR reacting system. C_{in} H_2O=5 %, C_{in} O_2=8 %, C_{in} NH_3=500 ppm, C_{in} NO_x=500 ppm, NO_2/NO_x=1. **a** N_2O formation with and without soot; **b** NO_x conversion with and without soot

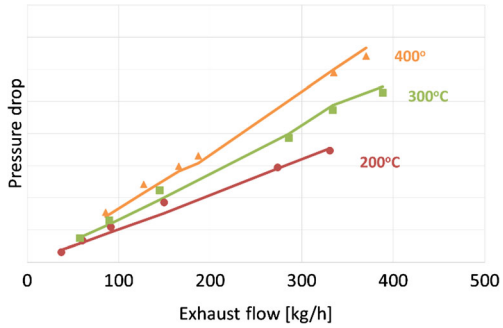

Fig. 9 Measured (*symbols*) and simulated (*continuous line*) clean filter pressure drop, at various flow rates and temperatures

only NO_x species: Fig. 7d confirms the drop of the soot combustion activity in the low–medium temperature range in the presence of both NO_2 and NH_3. The obvious explanation of the negative impact of NH_3 on the low-T soot combustion activity is that NO_2, i.e., the preferred oxidizing agent of soot at low temperatures, is prevented to react with soot when NH_3 is present, being converted instead in NH_3-SCR reactions, namely the fast SCR and the NO_2 SCR reactions. The present data therefore clearly and unambiguously demonstrate that $deNO_x$ reactions with NH_3 are the preferred reaction pathway for NO_2. Accordingly, a substantial reduction of the passive regeneration effect due to NO_2 can be expected in SDPF systems.

Finally, after addressing the impact of the $deNO_x$ reactions on soot combustion, also the impact of soot on the $deNO_x$ NH_3-SCR reactions was analyzed. In principle, in fact, the presence of particulate matter may affect all the SCR reactions. Our results, not shown here for the sake of brevity, indicate however that the presence of soot plays definitely a negligible role in NH_3 oxidation, standard and fast SCR reactions. Instead, soot can positively affect both the $deNO_x$ efficiency and the N_2O selectivity in the case of the NO_2 SCR conditions.

The results in Fig. 8 point out that soot lowered the N_2O formation between 250–400 °C and also had a great boosting effect on the NO_x conversion in the same temperature window. In principle, both phenomena can be explained by the NO_2-soot reactivity already observed in the low-temperature range. In the presence of excess NO_2, like for the conditions of Fig. 8, apparently the NO_2-activated soot combustion, reactions R.3 and R.4, can compete to some extent with the NH_3-SCR reactions: this results in converting a certain amount of NO_2 to NO, which shifts the actual NO_2/NO_x ratio from the original unit value to a more favorable value closer to the optimal 0.5 ratio of the fast SCR reaction [12], thus boosting the overall $deNO_x$ performances and lowering the N_2O selectivity.

As a final comment to the lab-scale study of the interactions between the chemistries of NH3-SCR and of soot combustion, it is worth noticing that all the dedicated runs were performed over physical mixtures comprising the powdered Cu-SDPF and the soot, i.e., in a configuration that emphasizes the interactions between the two reacting systems. In this configuration, in fact, the extent of such interactions is not limited by fluid dynamics or transport processes as indeed required for intrinsic kinetic modeling. The impact of such interactions in the case of the actual SDPF configuration, wherein the SCR catalyst washcoat and the soot layer are at least partially separated, will be examined in the next paragraphs.

3.2 Medium-Scale Engine Tests (PC)

3.2.1 Pressure Drop and Filtration Efficiency Calibration

The wall permeability of the clean filter was calibrated first. Simulation results, illustrated in Fig. 9, reveal excellent model prediction throughout the entire flow rate and temperature range tested.

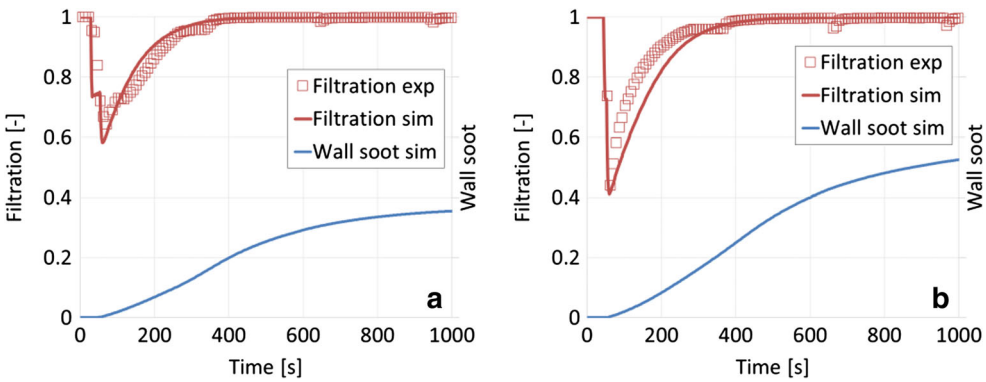

Fig. 10 Experimental (*symbols*) and simulated (*continuous line*) filtration efficiency and predicted wall soot mass at **a** 70 and **b** 230 kg/h

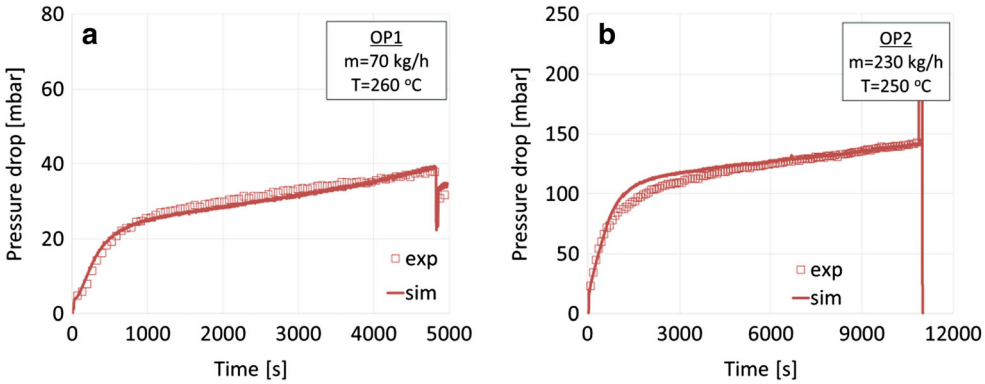

Fig. 11 Pressure drop experimental (*symbols*) and simulation (*continuous line*) results at **a** 70 and **b** 230 kg/h

Next, the pressure drop behavior of the loaded SDPF was examined. Soot loading experiments, starting from clean filter state, were performed at three different flow rates in order to capture a wide range of operating conditions. Filtration efficiency parameters were calibrated firstly, in order to obtain an accurate estimation of the soot mass that is deposited inside the wall. Simulation results, presented in Fig. 10, show a correct prediction in both the low and high flow rate regimes.

Finally, loaded wall and soot permeabilities were identified to accurately predict the pressure drop evolution with increasing soot loading at both low and high exhaust flow rates shown in Fig. 11.

3.2.2 Effect of NH_3 on Soot Oxidation

Soot oxidation reaction kinetics were calibrated from passive regeneration experiments, without NH_3 presence, performed at 350 and 450 °C. Kinetic parameters of soot reactions with O_2 and NO_2 were adjusted in order to accurately predict the burned soot mass, as well as the NO_2 consumption due to the C + NO_2 reactions.

In order to investigate the possible effect of SCR activity on passive regeneration, two additional passive regeneration tests were performed (refer to Table 1). The latter were exactly the same as the tests used for soot oxidation calibration (same initial soot loading, inlet conditions, and test duration), but NH_3 was now included in the exhaust stream. The NH_3/NO_x ratio was set to 1.05. A summary of the measured and simulated soot mass, for the above-mentioned passive regeneration tests, is presented in Fig. 12.

Focusing on the experimental results, it is evident that SCR activity has a negative effect on passive regeneration as the measured burned soot mass is lower for the cases when NH_3 is present. This negative effect is quantitatively much less compared to the results of the micro-reactor tests (refer to Fig. 7), a fact which can be attributed to the different experimental conditions. In micro-reactor tests, soot forms a physical mixture with the catalytic material, while in engine dyno tests, soot is deposited as a layer on the filter channels.

By simply combining the SCR reaction kinetics (obtained from micro-reactor tests) and the soot oxidation kinetics, the SDPF model is able to accurately capture the SCR effect on

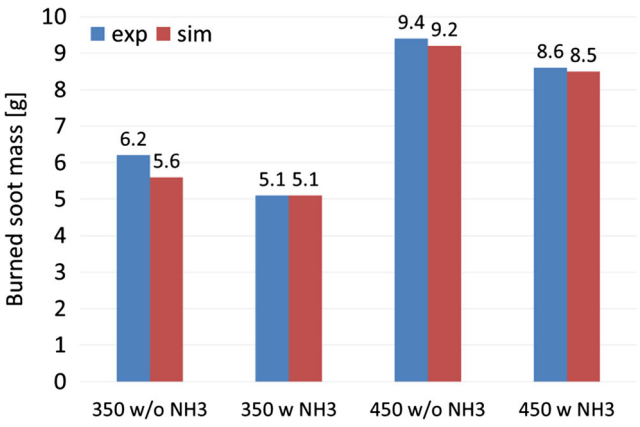

Fig. 12 Measured and simulated oxidized soot mass for passive regeneration experiments, with and without NH_3 injection, at 350 and 450 °C

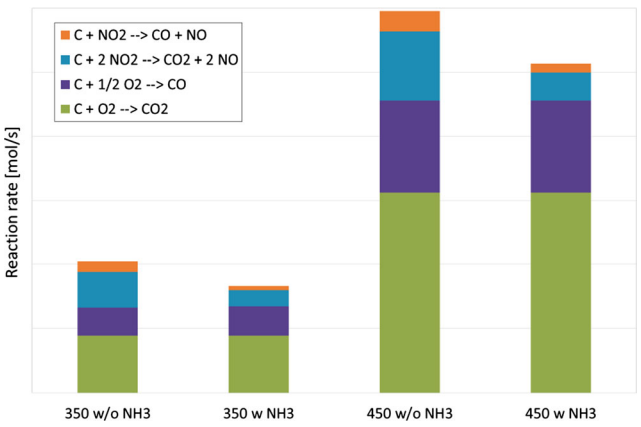

Fig. 13 Predicted soot oxidation reaction rates for passive regeneration experiments with and without NH_3 injection, at 350 and 450 °C

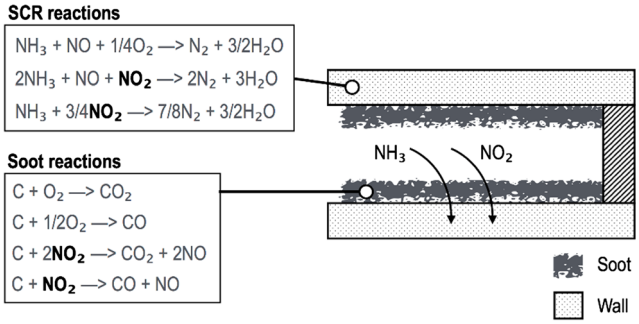

Fig. 14 Competition between soot oxidation and deNO$_x$ reactions

passive regeneration (see Fig. 12) without requiring any further recalibration. Analysis of simulation data reveals that in presence of deNO$_x$ activity, the total soot reaction rate is always lower for both 350 and 450 °C, as demonstrated in Fig. 13. For the same temperature, the contribution of C + O$_2$ reactions remains practically unchanged, while the reaction rate of C + NO$_2$ reactions is significantly lower. Indeed, a part of NO$_2$ is preferably reduced by NH$_3$ instead of reacting with soot, resulting in lower soot oxidation rates.

The above-mentioned competition between SCR and soot oxidation reactions for the consumption of NO$_2$ is schematically illustrated in Fig. 14.

In order to understand the computed behaviors, radial NO$_2$ profiles during passive regeneration at 450 °C were analyzed, both in presence and absence of NH$_3$. Figure 15a shows the computed NO$_2$ concentration in the soot and wall layers for the inlet SDPF channel, while in Fig. 15b, radial NO$_2$ profiles are given for a fixed axial location. When ammonia is not included in the exhaust gas, NO$_2$ generated from NO oxidation inside the catalytic wall diffuses back to the soot layer. In this case, there is always sufficient NO$_2$ content across the cake to oxidize soot. On the opposite, when NH$_3$ is present, soot oxidation rate is limited by reduced NO$_2$ concentrations resulting from NO$_2$ consumption by SCR reactions inside the wall, as well as from the "forward-diffusion" phenomena due to the generated concentration gradient in the flow direction.

3.3 Adjustment to Non-Road Application

Due to the fact that the DPF substrate used in the experiments with a MTU non-road engine differs from the one used during the medium-scale engine tests, the SDPF model could not be adopted without any changes.

Changes in substrate material and geometrical properties, as well as the soot which originates from different engines, cause a necessity of model recalibration in order to match the full-scale measuring data.

Similar to the calibration procedure described in the medium-scale engine tests, a run at different mass flow rates and temperatures (see Fig. 16a) was used for the calibration of the clean filter wall permeability with the result shown in Fig. 16b. Without any further changes in the model, it was able to predict both the NH$_3$ and NO$_x$ conversion during this experiment (see Fig. 16c–f). The model predicts slightly faster NH$_3$ breakthrough than the measured one (see Fig. 16c). This behavior is addressed to the long transfer lines between sampling point and analyzer and additional NH$_3$ adsorption in the lines. Figure 16e illustrates a slightly erroneous prediction of NO$_2$ concentration. Other experimental data, which are not shown here for the sake of brevity, show an overestimation of the NO oxidation rate.

In order to match the filtration efficiency (Fig. 18f) and the pressure drop distribution during the accelerated soot-loading experiments (the first 4500 s are shown in Fig. 18b, h), the loaded wall and soot cake permeabilities, as well as the filtration parameters, had to be refitted.

Next, the soot-burning kinetic parameters had to be adjusted in order to fit measured distribution of the pressure drop during soot oxidation period, as well as the weighted soot amount in the end (shown in Fig. 17b, without NH$_3$ dosing, but still with low soot amount coming into the DPF from engine). This was expected, since the measured oxygen reactivity of the two soot samples showed clearly different behavior (see Fig. 18).

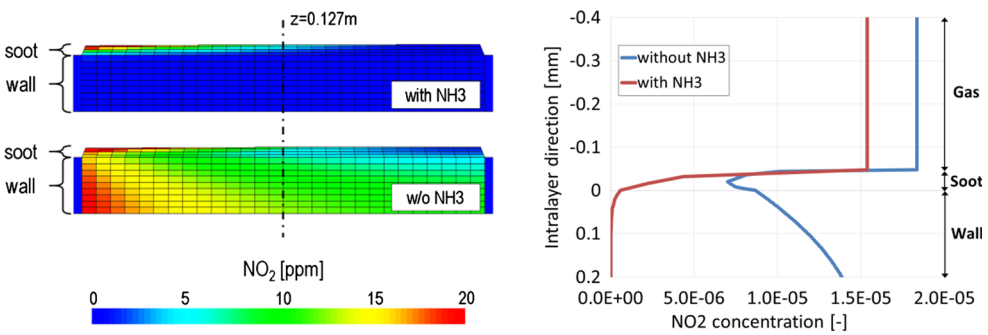

Fig. 15 NO$_2$ concentration profiles in soot and wall layer during passive regeneration at 450 °C **a** across the inlet channel and **b** for a fixed axial location (z=0.127 m)

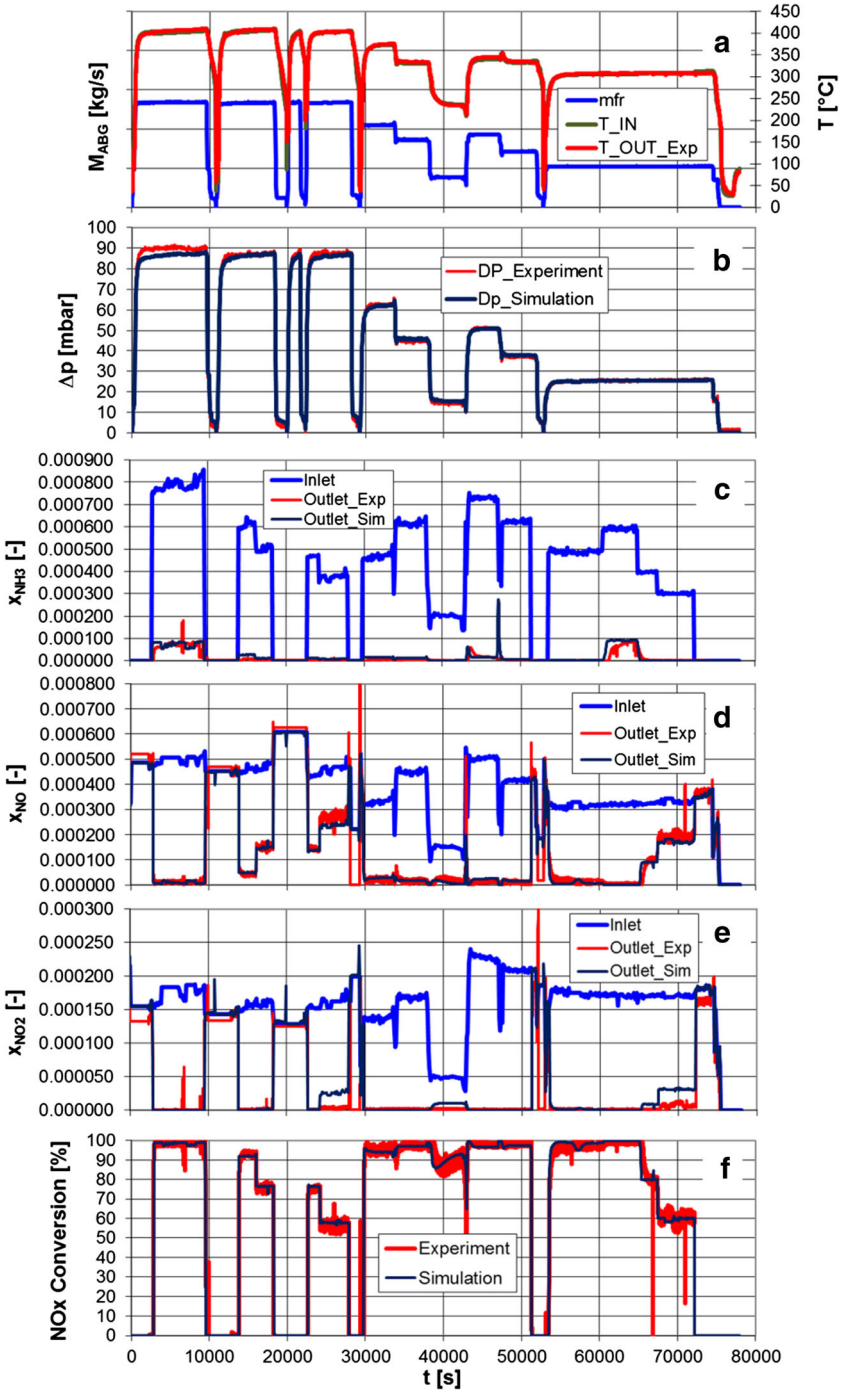

Fig. 16 Comparison between engine test bench measuring data and simulation. **a** Exhaust mass flow rate and temperature, **b** pressure drop, **c** NH_3 upstream and downstream mole fraction, **d** NO upstream and downstream mole fraction, **e** NO_2 upstream and downstream mole fraction, and **f** NO_x conversion rate

Furthermore, other engine test bench experiments, in which NO_2 supply was varied at constant temperature and soot amount, indicate a presence of two further soot-burning reactions, in which NO_2 is acting solely as a catalyst, but is not consumed, additionally to the reactions R.3 and R.4. This has already been described elsewhere [15]:

$$C + \frac{1}{2}O_2 + (NO_2) \rightarrow CO + (NO_2) \quad \text{(R.5)}$$

$$C + O_2 + (NO_2) \rightarrow CO_2 + (NO_2) \quad \text{(R.6)}$$

Not only the pressure drop decrease, but also the measured NO_2 consumption (see Fig. 17e), and CO increase as one of the soot combustion products (see Fig. 17c) clearly identify the soot burning is taking place.

On the contrary, in presence of NH_3 (shown in Fig. 17i, analog to Fig. 17b with low soot amount

coming into the DPF from engine), both the measured and the simulated pressure drop and soot amount decrease are much lower than it was the case in the experiment without NH_3 (compare Fig. 17b, i). Furthermore, the CO concentration drop downstream the SDPF at about t=6000 s (start of NH_3 dosing), denotes much lower soot combustion rate, compared to the experiment without NH_3 (see Fig. 17c, j). This is qualitatively in line with the observations made both in the micro-scale reactor and in the medium-scale engine test bench experiments. But, since MTU soot showed clearly lower reactivity with oxygen (see Fig. 18), the rates of the oxygen-based soot-burning reactions (R.1 and R.2) represent much lower portions in the overall soot-burning reaction rate, than it was the case with LAT-soot (compare Fig. 17g, n with Fig. 13).

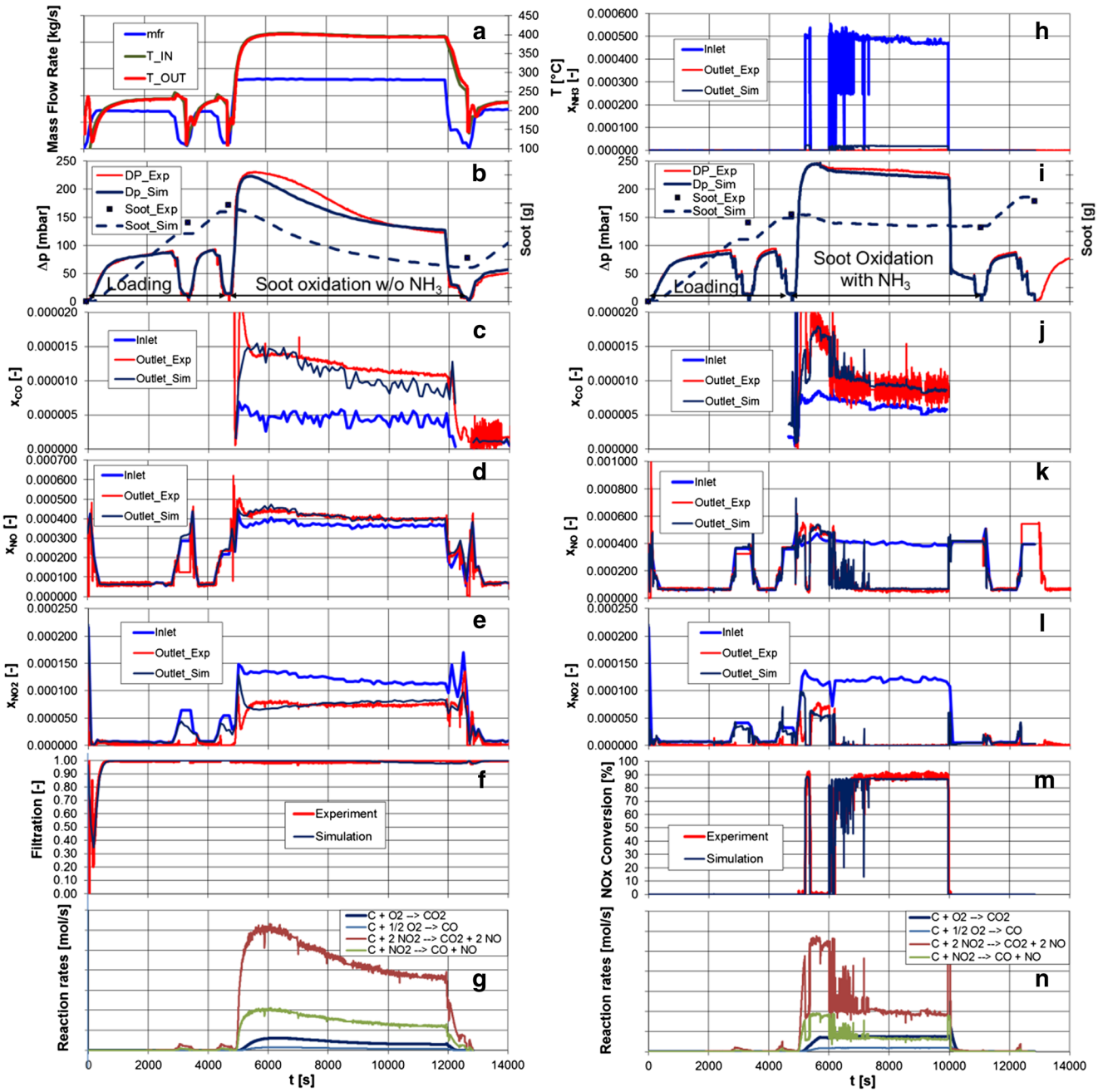

Fig. 17 SDPF without (*left side*) and with NH_3 dosing (*right side*): **a** mass flow rate and temperature, **b** pressure drop and soot loading, **c** CO mole fraction during soot oxidation, **d** NO mole fraction, **e** NO_2 mole fraction, **f** filtration efficiency, **g** soot oxidation reaction rates, **h** NH_3 mole fraction, **i** pressure drop and soot loading, **j** CO mole fraction during soot oxidation, **k** NO mole fraction, **l** NO_2 mole fraction, **m** NO_x conversion rate, and **n** soot oxidation reaction rates

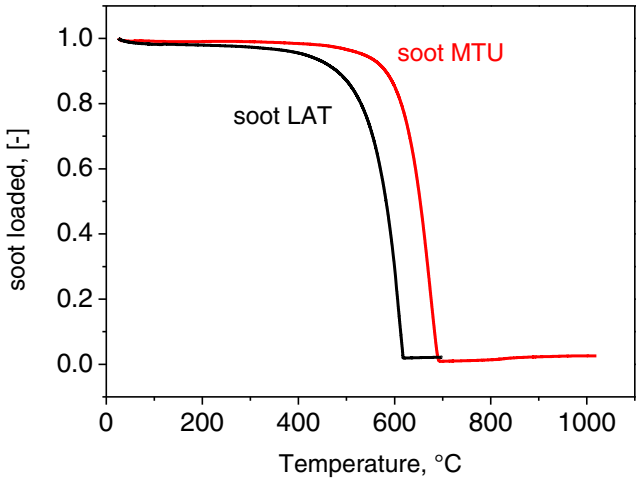

Fig. 18 DTA-TG in air: comparison of LAT and MTU soot samples

Consequently, with MTU soot, a much bigger difference in the burned soot amount with and without NH_3 dosing was to be expected. Indeed, in presence of NH_3, the weighted soot amount in the SDPF is only slightly lower than at the end of the loading interval (Fig. 17i), whereas in absence of NH_3, it was halved (Fig. 17b). The measured pressure drop and CO and NO_2 distributions support this observation. Finally, the model is able to take the presence of NH_3 into account without any further adjustments. The mechanism for this is described in Fig. 15.

4 Summary and Conclusions

A systematic bottom-up methodology to study and quantify the interactions of soot oxidation and SCR chemistry occurring on SDPFs was conducted. Lab-scale kinetic runs under conditions free of transport limitations clearly pointed out that the addition of NH_3 greatly reduces the low-temperature combustion of soot by NO_2. Under these operating conditions, in fact, the fast SCR and NO_2 SCR reactions successfully compete with soot combustion for NO_2 usage, being actually the NO_2-preferred reaction pathway. On the other hand, also the impact of soot on the SCR reactions has been investigated. The results show that presence of soot has a marginal influence on the NH_3 oxidation, standard SCR and fast SCR activities, while the SCR activity in excess of NO_2 is promoted due to the low-temperature interaction between NO_2 and soot, which leads to a more favorable NO_2/NO ratio, closer to the optimal 1/1 M ratio.

Intrinsic reaction kinetics obtained over powdered catalysts were successfully directly transferred into a physicochemical model of the flow, transport and reaction processes in wall-flow monolith channels. The expected negative influence of NH_3-SCR reactions on the soot oxidation rate was observed and modeled assuming a simple superposition of SCR and soot oxidation chemistries.

This allows for a straightforward decoupled model calibration process which can be used to develop efficient system design and dosing control methodologies.

Detailed analysis of the simulation results revealed the role of NO_2 competition between the soot layer and the coated wall, as well as the influence of intra-layer species diffusion processes that influence this competition.

The model was further applied to a much larger SDPF scale relevant for non-road engines. The necessary adaptations to the model parameters are mainly related to soot oxidation properties that may vary from one engine to another and wall permeability when choosing a different type of SDPF substrate.

Under all conditions tested, the influence of SCR reactions on passive soot oxidation has been shown to be quantitatively prominent, and therefore has to be carefully considered especially in applications which rely on continuous rather than active regeneration strategies. Model-based approaches are expected to support this complex system design and control problem enabling compact and efficient aftertreatment systems for the non-road engine industry.

Appendix

Wall-Flow Filter Model Equations

A schematic of the front and side view of a filter channel is given in Fig. 19. The governing equations for the conservation of mass, momentum, energy, and species are given in the following sub-sections.

Mass-Momentum Balance

Conservation of Mass of Channel Gas The mass balance equation for the gas flowing in the inlet and outlet channels is as follows:

$$\frac{\partial}{\partial z}\left(d_i^2 \rho_i v_i\right) = (-1)^i \cdot 4 d \rho_w v_w. \tag{E.2}$$

Conservation of Axial Momentum of Channel Gas Considering the mass gain/loss through the porous wall and the friction in the axial direction z, the momentum balance of the exhaust gas can be written as follows:

$$\frac{\partial p_i}{\partial z} + \frac{\partial}{\partial z}\left(\rho_i v_i^2\right) = -\alpha_1 \mu v_i / d_i^2. \tag{E.3}$$

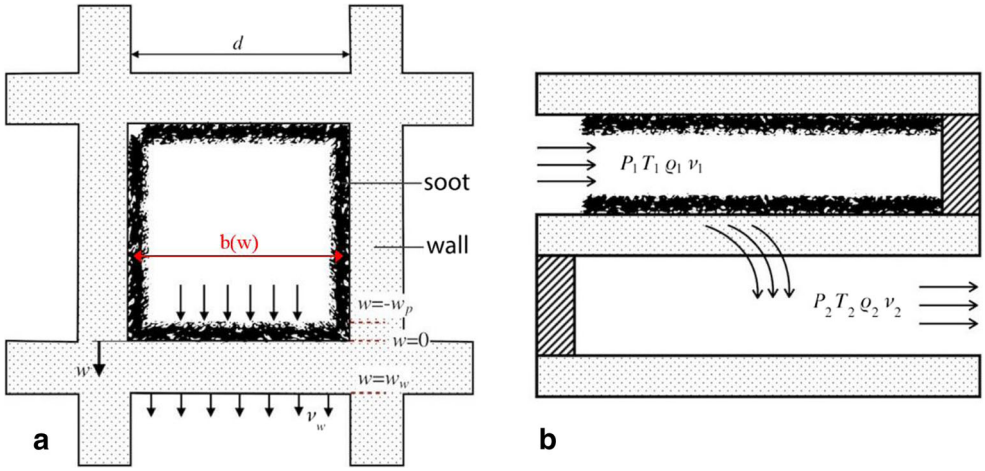

Fig. 19 Schematic of a filter channel. **a** Front and **b** side views

Pressure Drop To solve the velocity and pressure distribution in the inlet and outlet channels, it is necessary to calculate the pressure drop through the soot layer and the porous filter wall.

With the definitions shown in Fig. 19, the channel width available to the flow is given by the following relationship:

$$b(w) = d - 2\left(w_p - w\right). \tag{E.4}$$

The particulate layer thickness w_p can be calculated from the following expression:

$$w_p = \frac{1}{2}\left(d - \sqrt{d^2 - \frac{2m_p}{\rho_p \cdot V_{\text{trap}} \cdot \text{cpsm}}}\right), \tag{E.5}$$

where V_{trap} is the "effective" volume of the trap, excluding any cement and the plug length at the inlet and outlet of the filter.

Starting from the elementary Darcy law, the differential pressure drop over dw will be as follows:

$$\frac{\mathrm{d}p}{\mathrm{d}w} = \frac{\mu \cdot v(w)}{k_p}. \tag{E.6}$$

Although mass flow rate is steady throughout the soot layer, the gas velocity varies due to changes in gas density and flow area, as shown by the continuity equation:

$$v(w) = \frac{\rho_w \cdot v_w \cdot d}{\rho(w) \cdot b(w)}. \tag{E.7}$$

The gas density across the soot layer is a function of the local pressure. With the assumption of ideal gas, the density can be expressed as the following:

$$\rho(w) = \frac{p(w) \cdot M_g}{\mathrm{RT}}. \tag{E.8}$$

The permeability of the particulate deposit is dependent on the gas mean free path due to slip phenomena. The present model relies on the following expression [16]:

$$k_p = k_{p,0}\left(1 + C_4 \frac{p_0}{p}\mu\sqrt{\frac{T}{M_g}}\right). \tag{E.9}$$

The above formula expresses the dependency of soot permeability on local temperature and pressure for a constant soot density. The parameters $k_{p,0}$ and C_4 are estimated based on experimental data. Integration of E.6 provides the pressure drop over the soot layer thickness, taking into account E.7–E.9:

$$\Delta p_{\text{soot}} = \frac{\mathrm{RT}\ \mu d \rho_w v_w}{M_g \overline{p}\ 2k_p(\overline{p})} ln\left(\frac{d}{d - 2w_p}\right), \tag{E.10}$$

where $\overline{p}$ is the mean value of inlet and outlet pressures.

The pressure drop through the porous filter wall, assuming constant flow velocity across the wall, can be described by the Darcy law:

$$\Delta p_{\text{wall}} = \frac{\mu v_w}{k_w} w_w. \tag{E.11}$$

The dependence of wall permeability on temperature and pressure is taken into account, similarly to E.17. Furthermore, an extra correction is included to account for the sudden

decrease of wall permeability at the initial stage of soot loading, as soot particles block a portion of the wall pores:

$$k_w = \frac{1}{\frac{1}{k_{w,0}} + C_1\rho_p + C_2\rho_p^2}\left(1 + C_4\frac{p_0}{p}\mu\sqrt{\frac{T}{M_g}}\right). \quad \text{(E.12)}$$

The clean wall permeability $k_{w,0}$ and parameters C_1 and C_2 define a trinomial function of ρ_p which is defined as total soot accumulated in the wall per wall volume. In order to calculate the extra parameters, the following values are estimated based on experimental data:

- Clean wall permeability $k_{w,0}$
- Loaded wall permeability $k_{w,1}$ at reference soot loading $\rho_{p,1}$

Based on the above analysis for the wall and deposit layer, the pressure drop between the inlet and the outlet channel is the following:

$$p_1 - p_2 = \Delta p_{\text{soot}} + \Delta p_{\text{wall}}. \quad \text{(E.13)}$$

Energy Balance

Energy Balance of the Gas Phase The conservation of energy of the channel gas has two expressions, one for the inlet (E.14) and one for the outlet channel (E.15).

$$C_{\text{p,g}}\rho_1 v_1\big|_z\frac{\partial T_1}{\partial z} = h_1\frac{4}{d_1}(T_s - T_1) \quad \text{(E.14)}$$

$$C_{\text{p,g}}\rho_2 v_2\big|_z\frac{\partial T_2}{\partial z} = \left(h_2 + C_{\text{p,g}}\rho_w v_w\right)\frac{4}{d}(T_s - T_2) \quad \text{(E.15)}$$

Energy Balance of the Solid Phase The temperature field in the filter is described by the transient heat conduction equation with heat sources in axi-symmetric coordinates:

$$\rho_{\text{s}}\cdot C_{\text{p,s}}\frac{\partial T_{\text{s}}}{\partial t} = \lambda_{\text{s},z}\frac{\partial^2 T_{\text{s}}}{\partial z^2} + S. \quad \text{(E.16)}$$

The source term S includes the contribution of the convective heat transfer of the gas flow in the channel H_{conv} and through the wall H_{wall}, as well as the exothermic heat release H_{react}.

$$S = H_{\text{conv}} + H_{\text{wall}} + H_{\text{react}} \quad \text{(E.17)}$$

$$H_{\text{conv}} = h_1\cdot S_{\text{F}}\cdot(T_1 - T_s) + h_2\cdot S_{\text{F}}\cdot(T_2 - T_s) \quad \text{(E.18)}$$

$$H_{\text{wall}} = \rho_{\text{w}}\cdot v_{\text{w}}\cdot S_{\text{F}}\cdot C_{\text{p,g}}\cdot(T_1 - T_s) \quad \text{(E.19)}$$

$$H_{\text{react}} = S_{\text{F}}\sum_k\left(\int_{-w_p}^{w_{\text{w}}} f_w R_k \,\text{d}w\right)\cdot\Delta H_k \quad \text{(E.20)}$$

The definition of the geometrical parameter f_w is as follows:

$$f_w = \frac{b(w)}{d}. \quad \text{(E.21)}$$

Species Balance

The importance of species transfer to account for oxygen convection to the reacting soot layer was recognized in [17]. In addition, the solution of the species transfer equation is essential to model the catalyzed filters with respect to pollutant conversion and their interactions with the accumulated soot.

The governing advection-reaction-diffusion equation for the conservation of mass of any species within the soot layer and wall is as follows:

$$v_w\frac{\partial y_j}{\partial w} - D_{w,j}\frac{\partial}{\partial w}\left(f_w\frac{\partial y_j}{\partial w}\right) = \frac{f_w}{c_m}\sum_k n_{j,k}R_k. \quad \text{(E.22)}$$

The calculation of the effective diffusivity $D_{w,j}$ is based on the mean transport pore model which uses the following expression:

$$\frac{1}{D_{w,j}} = \frac{\tau}{\varepsilon_{\text{pore}}}\left(\frac{1}{D_{\text{mol},j}} + \frac{1}{D_{\text{knud},j}}\right), \quad \text{(E.23)}$$

with the Knudsen diffusivity:

$$D_{\text{knud},j} = \frac{d_{\text{pore}}}{3}\sqrt{\frac{8\text{RT}}{\pi M_j}}. \quad \text{(E.24)}$$

The porosity $\varepsilon_{\text{pore}}$ and the mean pore size d_{pore} can be extracted from the micro-structural properties of the washcoat while tortuosity τ is an empirical parameter.

The boundary conditions couple the wall with the gas concentrations in the channels. The "film" approach is used to compute the convective mass transfer from the bulk gas to the wall surface. The mass transfer

coefficients $k_{i,j}$ correspond to laminar flow for both inlet and outlet channels:

$$\frac{\partial\left(v_1 y_{1,j}\right)}{\partial z} = -\frac{4}{d \cdot {f_w}^2} v_w y_{1,j} + \frac{4}{d \cdot f_w} k_{1,j}\left(y_{1s,j} - y_{1,j}\right) \quad \text{(E.25)}$$

$$\frac{\partial\left(v_2 y_{2,j}\right)}{\partial z} = \frac{4}{d \cdot {f_w}^2} v_w y_{2s,j} + \frac{4}{d \cdot f_w} k_{2,j}\left(y_{2s,j} - y_{2,j}\right) \quad \text{(E.26)}$$

References

1. Tan, J., Solbrig, C., Schmieg, S.: The development of advanced 2-way SCR/DPF systems to meet future heavy-duty diesel emissions. SAE Technical Paper. 2011-01-1140 (2011)
2. Naseri, M., Chatterjee, S., Castagnola, M., et al.: Development of SCR on diesel particulate filter system for heavy duty applications. SAE Technical Paper, 2011-01-1312 (2011)
3. Nova, I., Tronconi, E. (eds.): Urea-SCR technology for deNO_x aftertreatment of diesel exhausts. Fundamental and Applied Catalysis, Springer New York (2014)
4. Lee, J., Paratore, M., Brown, D.: Evaluation of Cu-based SCR/DPF technology for diesel exhaust emission control. SAE Technical Paper, 2008-01-0072 (2008)
5. Maunula, T.: Intensification of catalytic aftertreatment systems for mobile applications. SAE Technical Paper, 2013-01-0530 (2013)
6. Colombo, M., Koltsakis, G., Koutoufaris, I.: A modeling study of soot and deNO_x reaction phenomena in SCRF systems. SAE Technical Paper, 2011-37-0031 (2011)
7. Watling, T.C., Ravenscroft, M.R., Avery, G.: Development, validation and application of a model for an SCR catalyst coated diesel particulate filter. Catal. Today **188**, 32–41 (2012)
8. Schrade, F., Brammer, M., Schaeffner, J., et al.: Physico-chemical modeling of an integrated SCR on DPF (SCR/DPF) system. SAE Technical Paper, 2012-01-1983 (2012)
9. Nova, I., Ciardelli, C., Tronconi, E., Chatterjee, D., Bandl-Konrad, B.: NH_3-SCR of NO over a V-based catalyst: low-T redox kinetics with NH_3 inhibition. AIChE J **52**, 3222–3233 (2006)
10. Chatterjee, D., Burkhardt, T., Weibel, M., Tronconi, E., Nova, I., Ciardelli, C.: Numerical simulation of NO/NO_2/NH_3 reactions on SCR-catalytic converters: model development and applications. SAE Technical Paper, 2006-01-0468 (2006)
11. Colombo, M., Nova, I., Tronconi, E., Schmeißer, V., Bandl-Konrad, B., Zimmermann, L.: NO/NO_2/N2O–NH_3 SCR reactions over a commercial Fe-zeolite catalyst for diesel exhaust aftertreatment: intrinsic kinetics and monolith converter modeling. Appl. Catal. B Environ. **111–112**, 106–118 (2012)
12. Colombo, M., Nova, I., Tronconi, E.: A comparative study of the NH_3-SCR reactions over a Cu-zeolite and a Fe-zeolite catalyst. Catal. Today **151**, 223–230 (2010)
13. Setiabudi, A., Makkee, M., Moulijn, J.A.: The role of NO_2 and O_2 in the accelerated combustion of soot in diesel exhaust gases. Appl. Catal. B Environ. **50**, 185–194 (2004)
14. Stanmore, B.R., Tschamber, V., Brilhac, J.F.: Oxidation of carbon by NO_x, with particular reference to NO_2 and N_2O. Fuel **87**, 131–146 (2008)
15. Jeguirim, M., Tschamber, V., Brilhac, J.F.: Kinetics of catalyzed and non-catalyzed soot oxidation with nitrogen dioxide under regeneration particle trap conditions. J. Chem. Technol. Biotechnol. **84**(5), 770–776 (2009)
16. Pulkrabek, W., Ibele, W.: The effect of temperature on the permeability of a porous material. Int. J. Heat Mass Transf. **30**, 1103–1109 (1987)
17. Haralampous, O., Koltsakis, G.: Intra-layer temperature gradients during regeneration of diesel particulate filters. Chem. Eng. Sci. **57**, 2345–2355 (2002)